Supporting Information

Guillemot et al. 10.1073/pnas.1207658109

SI Text

I. Materials. ***A. Synthesis.*** The three mesoporous materials studied in this work are hexagonal-ordered mesoporous silicas.

MCM-41 (Mobil Crystalline Material 41) (1) is a model material: it presents independent cylindrical pores that are hexagonally ordered and a narrow pore-size distribution. For our study, we synthesized an MCM-41 formed from the structuring agent octadecyltrimethyl ammonium bromide ($C_{18}NMe_3Br$) in basic conditions at 115 °C for 24 h. The protocol used is detailed in the text (2).

SBA-15 (Santa Barbara Amorphous 15) (3) also has cylindrical pores in hexagonal arrangement, but contrary to MCM-41, these mesopores can be interconnected by a secondary pore network. According to the synthesis temperature, we are able to control the formation of this secondary pore network. To study a SBA-15 close to a model material, we chose a synthesis temperature of 60 °C, which prevents the secondary network of micropores from expanding and creating interconnections between pores (4). The SBA-15 studied was structured with a triblock poly(ethylene oxide)-poly(propylene oxide)-poly(ethylene oxide) copolymer ($EO_{20}PO_{70}EO_{20}$) under acidic medium at 60 °C for 24 h. The protocol is detailed in ref. 4.

The third material studied in this work is an HMS (Hexagonal Mesoporous Silica) (5). It shows a principle hexagonal pore network that can randomly be connected in a few locations. Therefore, this material is a bit less ordered than MCM-41. It was prepared with $CN_{16}H_2$ as the structuring agent, with a ratio EtOH/H_2O = 0.19 at T_{amb} for 24 h. The synthesis protocol is described in the text (6).

The three mesoporous silicas were silanized by grafting chlorodimethyloctylsilane. The reaction was carried out in anhydrous refluxing toluene containing pyridine under nitrogen for 15 h at 120 °C. The functionalization protocol applied is explained in ref. 7.

B. Materials characteristics. The three ordered mesoporous silicas before and after silanization were characterized by nitrogen adsorption at 77 K with a Micromeritics ASAP 2000 apparatus. The isotherms are presented in Fig. S1.

Table S1 summarizes the textural properties of the parent and grafted materials determined from the nitrogen sorption isotherms. The Broekhoff–de Boer method (BdB) was chosen to calculate the pore radius of the parent materials (8). This method was, indeed, shown to be the most appropriate to determine the pore size of siliceous materials (9). The as-synthesized MCM-41 has a Brunauer–Emmett–Teller (BET) surface area of 847 m^2/g and a BdB pore radius of 2.07 nm. The as-synthesized SBA-15 presents a BET surface area of 702 m^2/g and a BdB pore radius of 3.15 nm. The as-synthesized HMS presents a BET surface area of 935 m^2/g and a BdB pore radius of 2.24 nm (Table S1).

To evaluate the pore size of the grafted materials, we calculate two pore radii using the BdB method and the Barret–Joyner–Halenda method, which is one of the most used methods (10). These methods provide upper and lower bounds of the pore size for the silanized materials. For our study, we took the mean of these two radii, R_{ads}.

The values of the intrusion and extrusion pressures of water in the grafted materials measured in our experiments in quasistatic conditions (that is, with t_{ext} = 10 s) are reported in Table S2.

II. Influence of a Wall Defect on the Nucleus Energy. We first consider a localized bump in the form of a half-sphere of radius R_{def} on the wall of the cylindrical pore (Fig. S2). The defect lowers the energy of a vapor nucleus by increasing the area of the hydrophobic surface compared with the pore wall and by decreasing the nucleus volume. The classical energy barrier is

$$\Delta\Omega = P_L K_1(\theta) R_p^3 + \gamma_{lv} K_2(\theta) R_p^2 - \Delta\Omega_{def}$$

and

$$\Delta\Omega_{def} = (\gamma_{sl} - \gamma_{sv}) \times (A_{def} - A_{wall}) + P_L V_{def},$$

where A_{def} is the area of the sphere portion inside the cylinder, A_{wall} is the area of the sphere intersection with the wall, V_{def} is the portion of the sphere volume inside the cylinder, and $P_L = P_{ext}$ is the water pressure at extrusion.

Clearly, $A_{def} < 2\pi R_{def}^2$ and $A_{wall} > \pi R_{def}^2$, and therefore, $A_{def} - A_{wall} < \pi R_{def}^2$ and $V_{def} < 2\pi R_{def}^3/3$. We know the value of $\gamma_{sl} - \gamma_{sv}$ from the intrusion pressure (Eq. **1**): $(\gamma_{sl} - \gamma_{sv}) = R_p P_{int}/2$. We get

$$\Delta\Omega_{def} < \frac{P_{int}}{2}\pi R_{def}^2 R_p + \frac{2P_{ext}}{3} R_{def}^3.$$

With $R_{def} = R_p$, we get $\Delta\Omega > 80\ k_BT$ for the MCM-41, $\Delta\Omega > 130\ k_BT$ for the SBA-15, and $\Delta\Omega > 110\ k_BT$ for the HMS at T = 50 °C. The value needed for the standard model of nucleation is $\Delta\Omega = \ln(t_{ext}L/b\tau)k_BT \sim 50\ k_BT$ (changing the ratio $t_{ext}L/b\tau$ by a factor 10 changes $\Delta\Omega$ by only 2.3 k_BT). Thus, even such a large wall defect is far from being able to provide nucleation.

We then consider a large constriction in the form of a cylinder of radius R_{def}. By replacing R_p with R_{def} in Eq. **4**, one can calculate the R_{def} value needed to provide the extrusion pressure and then, calculate self-consistently the intrusion pressure $P_{int}(R_{def})$ needed to force water in this narrow portion of cylinder. For instance, at 50 °C, one finds R_{def} = 0.78 nm for MCM-41 leading to $P_{int}(R_{def})$ = 760 bars; in SBA-15, R_{def} = 0.89 nm for leading to $P_{int}(R_{def})$ = 740 bars, and in HMS, R_{def} = 0.79 nm and $P_{int}(R_{def})$ = 726 bars. These pressures are never reached in the experiment.

III. Nucleation Theory in a Cylinder with Line Tension. The nucleation barrier that controls the formation of a bubble in a cylindrical pore corresponds to the saddle point of the grand canonical potential landscape that the system has to cross on its way from the liquid to the vapor phase. Because the saddle point is an extremum of the grand canonical potential, it corresponds to an equilibrium (but unstable) state. A simple way to calculate the nucleation barrier is, thus, to generate a path of equilibrium states that bridges the liquid and vapor phases. The barrier corresponds to the maximum of the grand canonical potential along this path. Getting equilibrium states for a bubble in a cylinder with line tension is a nonstandard task, and approximate treatments have been done in a previous study (11). The path used to compute the barrier was generated without line tension, and the line tension contribution was simply added to the grand canonical potential a posteriori by computing the contact line length. This result adds a term $\tau K_3(\theta) R_p$ to the critical nucleus energy, with $K_3(\theta)R_p$ the perimeter of the nucleus contact line calculated without line tension. This approximate scheme is Eq. **6**. The values of the functions K_1, K_2, and K_3 calculated in ref. 11 are reproduced hereafter (Table S3).

This procedure is expected to overestimate the nucleation barrier, because the path does not strictly cross the saddle point. To test the validity of this approach, we computed the path corresponding to the equilibrium shapes with line tension using a simple relaxation method. For each value of the bubble inter-

nal volume V, a triangulated mesh is generated initially as shown in Fig. S3, and an iterative procedure is applied to get the equilibrium shape.

For a given step, the local curvature vector is computed for each vertex $\mathbf{r}_i$ using the equation (12)

$$\mathbf{K} = \frac{1}{2A_i}\sum_{j\in n_i}\left(\cot\alpha_{ij} + \cot\beta_{ij}\right)\left(\mathbf{r}_i - \mathbf{r}_j\right),$$

where n_i represents the set of neighboring sites (connected to site i by a link), and α_{ij} and β_{ij} are the two angles defined in Fig. S3. A_i is the area attributed to site i: it is computed by summing one-third of the area of the three triangles containing site i. The local curvature is obtained as

$$\begin{aligned} c(\mathbf{r}_i) = &-\|\mathbf{K}\| \text{ if } \mathbf{K}.\hat{\mathbf{n}} > 0 \\ &+\|\mathbf{K}\| \text{ otherwise} \end{aligned}$$

where $\hat{\mathbf{n}}$ is the normal vector in $\mathbf{r}_i$ pointing to the external medium. A sphere shall, thus, have a negative curvature with these conventions.

For a vertex in contact with the cylinder, the curvature of the contact line is computed as well by a finite difference of the tangential vector (leading directly to the curvature times the normal vector).

The forces caused by the surface and line tensions can thus be computed easily at each vertex from the knowledge of the normal vectors and the local curvatures as well as the force caused by the internal pressure. The vertices are then moved with a displacement proportional to the local forces (overdamped dynamics). The internal pressure of the drop is adjusted at each step to fix the internal volume V of the bubble. The procedure is repeated until a convergence of the grand canonical potential of the bubble is reached with a relative accuracy better than 10^{-6}.

The path corresponds to bubbles with growing volumes V with a maximum volume $V = 4.4R_p^3$, where a morphological transition to an axisymmetric bubble with lower energy occurs (11). The variation of $\Delta\Omega$ with V is plotted in Fig. 4 for various values of the liquid pressure P_L. The nucleation kernel corresponds to the maximum of these curves. Quite interestingly, most of the time, it corresponds to $V = 4.4R_p^3$. Thanks to this procedure, we could generate a path of equilibrium shapes accounting for the line tension (Fig. 4) and compare the energy barrier with the approximate scheme mentioned above (Fig. 6). The computations were done for the reduced line tension $\tau^* = \tau/\gamma_{lv}R_p = \pm 0.1$. The agreement between the approximate estimation (11) and the present work is impressive. Although the approximate theory overestimates the nucleation barrier slightly, as expected, the difference is, in general, barely visible.

1. Beck JS, et al. (1992) A new family of mesoporous molecular sieves prepared with liquid crystal templates. *J Am Chem Soc* 114:10834–10843.
2. Martin T, Galarneau A, Di Renzo F, Brunel D, Fajula F (2004) Great improvement of chromatographic performance using MCM-41 spheres as stationary phase in HPLC. *Chem Mater* 16(9):1725–1731.
3. Zhao D, et al. (1998) Triblock copolymer syntheses of mesoporous silica with periodic 50 to 300 angstrom pores. *Science* 279(5350):548–552.
4. Galarneau A, et al. (2003) Microporosity and connections between pores in SBA-15 mesostructured silicas as a function of the temperature of synthesis. *New J Chem* 27 (1):73–79.
5. Tanev PT, Pinnavaia TJ (1996) Mesoporous silica molecular sieves prepared by ionic and neutral surfactant templating: A comparison of physical properties. *Chem Mater* 8(8):2068–2079.
6. Di Renzo F, et al. (1999) Textural control of micelle-templated mesoporous silicates: The effects of co-surfactants and alkalinity. *Microporous Mesoporous Mater* 28(3):437–446.
7. Martin T, et al. (2001) Towards total hydrophobisation of MCM-41 type silica surface. *Stud Surf Sci Catal* 135:4621–4628.
8. Broekhoff JCP, De Boer JH (1968) Studies on pore systems in catalysts: XIII. Pore distributions from the desorption branch of a nitrogen sorption isotherm in the case of cylindrical pores B. Applications. *J Catal* 10(4):377–390.
9. Galarneau A, Desplantier D, Dutartre R, Di Renzo F (1999) Micelle-templated silicates as a test-bed for methods of mesopore size evaluation. *Microporous Mesoporous Mater* 27:297–308.
10. Barrett EP, Joyner LG, Halenda PP (1951) The determination of pore volume and area distributions in porous substances. I. Computations from nitrogen isotherms. *J Am Chem Soc* 73(1):373–380.
11. Lefevre B, et al. (2004) Intrusion and extrusion of water in hydrophobic mesopores. *J Chem Phys* 120(10):4927–4938.
12. Taubin G (1994) Rasterizing algebraic curves and surfaces. *IEEE Comput Graph Appl* 14(2):14–23.

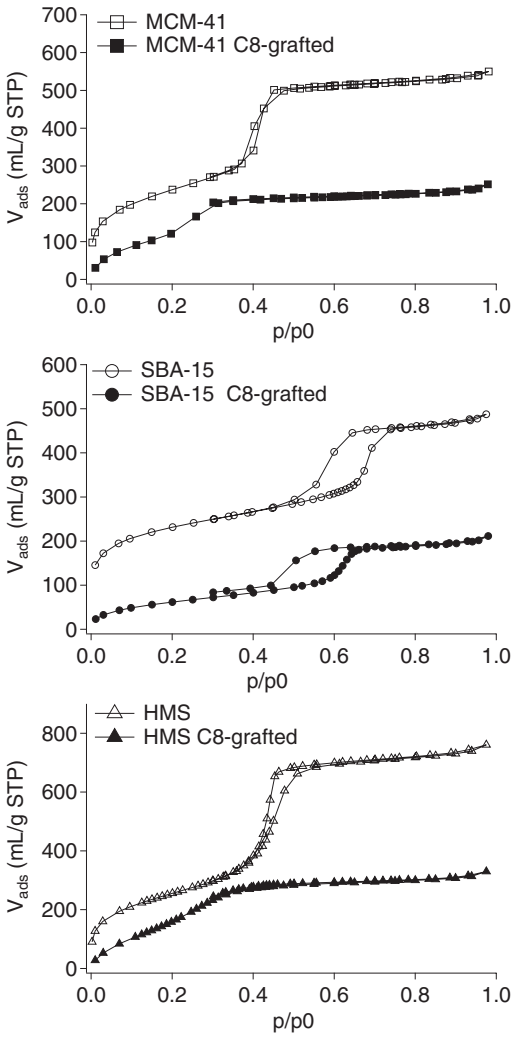

Fig. S1. Nitrogen adsorption–desorption isotherms for three both grafted (closed symbols) and parent (open symbols) mesoporous silicas MCM-41, SBA-15, and HMS. The surface functionalization is performed with chlorodimethyloctylsilane as grafting agent.

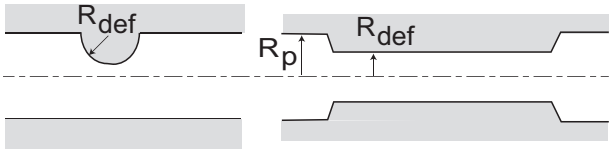

Fig. S2. (*Left*) Localized defect. (*Right*) Cylindrical pore constriction.

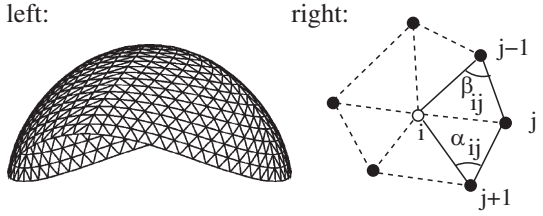

Fig. S3. (*Left*) Example of triangulated mesh used for the computation. The lower vertices are in contact with the cylinder. (*Right*) Angles used for curvature computation.

Table S1. Textural properties of the parent and grafted materials determined from nitrogen sorption analysis

	MCM-41	SBA-15	HMS
Parent materials			
S_{BET} (m^2/g)	847	702	935
V_p (mL/g)	0.79	0.71	1.06
R_{BdB} (nm)	2.07	3.15	2.24
C8-grafted materials			
S_{BET} (m^2/g)	495	234	726
V_p (mL/g)	0.33	0.29	0.44
R_{BJH} (nm)	1.25	1.91	1.44
R_{BdB} (nm)	1.43	2.40	1.64
R_{ads} (nm)	1.34	2.16	1.54

Table S2. Mean intrusion/extrusion pressures (in MPa) measured for quasistatic cycles (t_{ext} = 10 s)

	Intrusion pressure			Extrusion pressure		
T (°C)	MCM-41	SBA-15	HMS	MCM-41	SBA-15	HMS
20	44.1			11.6		
30	44.1		35.2	14.1		7.1
40	43.7		35.3	16.1		9.2
50	43.2	29.1	35.3	17.8	6.0	10.9
60	42.6	29.0	35.2	19.2	6.9	12.7
70		28.9	34.9		8.0	14.0
80		28.8			9.1	

Table S3. Functions appearing in Eqs. 4 and 6 as tabulated in ref. 1

	θ (°)							
	95	100	105	110	115	120	125	130
K_1	4.06	4.11	4.17	4.22	4.27	4.28	4.25	4.18
K_2	6.16	5.46	4.73	3.97	3.19	2.42	1.70	1.02
K_3	11.85	12.00	12.16	12.28	12.38	12.43	12.46	12.48

1. Lefevre B, et al. (2004) Intrusion and extrusion of water in hydrophobic mesopores. *J Chem Phys* 120(10):4927–4938.